Biomaterials Science

ROYAL SOCIETY OF CHEMISTRY

PAPER

View Article Online
View Journal | View Issue

Cite this: *Biomater. Sci.*, 2024, **12**, 4759

Controlling cellular packing and hypoxia in 3D tumor spheroids *via* DNA interactions†

Sven A. Saemundsson,[a] Shane D. Curry,[a] Bryce M. Bower,[a] Ethan J. DeBoo,[a] Andrew P. Goodwin [a,b] and Jennifer N. Cha *[a,b,c]

Received 17th May 2024,
Accepted 5th August 2024

DOI: 10.1039/d4bm00688g

rsc.li/biomaterials-science

Tumor spheroids represent valuable *in vitro* models for studying cancer biology and evaluating therapeutic strategies. In this study, we investigated the impact of varying lengths of DNA-modified cell surfaces on spheroid formation, cellular adhesion molecule expression, and hypoxia levels within 4T1 mouse breast cancer spheroids. Through a series of experiments, we demonstrated that modifying cell surfaces with biotinylated DNA strands of different lengths facilitated spheroid formation without significantly altering the expression of fibronectin and e-cadherin, key cellular adhesion molecules. However, our findings revealed a notable influence of DNA length on hypoxia levels within the spheroids. As DNA length increased, hypoxia levels decreased, indicating enhanced intercellular spacing and porosity within the spheroid structure. These results contribute to a better understanding of how DNA modification of cell surfaces can modulate spheroid architecture and microenvironmental conditions. Such insights may have implications for developing therapeutic interventions targeting the tumor microenvironment to improve cancer treatment efficacy.

Introduction

In this study, we explore the interplay between hypoxia, cellular adhesion molecules, and spheroid architecture within the context of 4T1 mouse breast cancer spheroids. Tumor microenvironments are complex ecosystems characterized by a myriad of cellular interactions and biochemical signaling pathways.[1–3] Three-dimensional cancer cell spheroids serve as invaluable experimental models in cancer research because they can recapitulate key aspects of tumor architecture and microenvironmental interactions, including cellular heterogeneity, spatial organization, and the presence of gradients in oxygen, nutrients, and signaling molecules.[4–6] Cancer cell spheroids are widely used for drug screening and therapeutic development, as they have the ability to model drug penetration, distribution, and cytotoxicity into tumors more effectively than 2D cells can.[7,8] Moreover, the incorporation of stromal cells, extracellular matrix proteins, and soluble factors within spheroids enables researchers to investigate the complex interplay between cancer cells and their surrounding milieu.[9–14] These models can also simulate various stages of tumor progression and metastasis, providing insights into the molecular mechanisms underlying these processes and identifying potential therapeutic targets.[11]

Hypoxia, or low oxygen tension, is a central factor in shaping the tumor microenvironment, exerting profound effects on cancer progression and therapeutic responses.[15,16] Under hypoxic conditions, tumor cells undergo adaptive responses mediated by hypoxia-inducible factors (HIFs), which regulate a wide array of genes involved in angiogenesis, metastasis, apoptosis resistance, and metabolic adaptation.[17–23] Importantly, hypoxia also influences the behavior of stromal cells within the tumor microenvironment, including cancer-associated fibroblasts (CAFs) and macrophages. Notably, hypoxia has been shown to stimulate the activation of CAFs and enhance their pro-tumorigenic functions, further exacerbating tumor aggressiveness.[24] Macrophages, on the other hand, exhibit remarkable plasticity and can adopt distinct phenotypes depending on the microenvironmental cues they encounter. For example, hypoxia has been shown to influence macrophage polarization towards the M2 or protumorigenic phenotype, fostering an immunosuppressive and tumor-promoting microenvironment.[25,26]

Understanding the impact of hypoxia on cellular behavior and tumor progression necessitates appropriate *in vitro* models that recapitulate the complexity of the tumor microenvironment. Tumor spheroids represent one such model,

[a]*Department of Chemical and Biological Engineering, University of Colorado, Boulder, 596 UCB, Boulder, CO, 80303, USA. E-mail: Jennifer.Cha@colorado.edu*
[b]*Materials Science and Engineering Program, University of Colorado, Boulder, 596 UCB, Boulder, CO, 80303, USA*
[c]*Biomedical Engineering Program, University of Colorado, Boulder, 596 UCB, Boulder, CO, 80303, USA*

† Electronic supplementary information (ESI) available. See DOI: https://doi.org/10.1039/d4bm00688g

offering spatial organization, cellular heterogeneity, and physiological gradients akin to those found *in vivo*.[14,27–30] In this study, we sought to elucidate the impact of changing DNA length on cell surfaces would have on hypoxia within spheroids. DNA is a widely-accepted, versatile tool that can provide precise control over the spatial arrangement of colloidal particles at the nano- or microscale by DNA complementarity.[31] By designing specific DNA sequences, researchers can dictate the morphology, composition, and functionality of assembled colloidal structures with unprecedented precision,[32] allowing the construction of 2- and 3D architectures with diverse functions, such as bio-recognition, sensing, and drug delivery.[33–36] In previous studies, we used DNA interactions to assemble cells into spheroids. Specifically, DNA oligonucleotides were attached to the cell receptors of MDA-MB-468 cancer cells and NIH/3T3 fibroblasts to induce the formation of mono- and coculture spheroids. As a result, the MDA-MB-468 cancer cells and NIH/3T3 cells packed in a homogeneous manner when hybridized with DNA, whereas cell sorting was clearly observed in the absence of DNA.[14,30] These results clearly demonstrated that DNA can be used to guide cell–cell interactions and thus assembly in 3D.

In this study, we use DNA's of different lengths to change cell–cell distance and spheroid 'porosity', then show the effects of different cell packing within the formed 3D spheroids. First, we demonstrate methods to produce biotinylated single stranded DNA (ssDNA) longer than what can be purchased (>100 bases). These strands were conjugated to 4T1 cancer cells, remained expressed up to 24 h, and hybridized to complementary DNA strands. Next, 3D 4T1 spheroids were produced using the different DNA lengths and tested for changes in cell–cell contacts and matrix proteins. Lastly, hypoxia levels within 4T1 mouse breast cancer spheroids were measured, which showed a significant decrease in hypoxia with increasing DNA length. These results show the intricate interplay between hypoxia, cellular adhesion, and tumor microenvironment dynamics, with implications for understanding cancer progression and therapeutic interventions.

Results and discussion

In prior studies, DNA hybridization was used to control packing in 3D mono- and coculture spheroids from MDA-MB-468 breast cancer and NIH/3T3 fibroblast cells.[14] Based on these results, it was further hypothesized that using DNA could be used to control the overall distance between cells. It is well accepted that in tumor microenvironments (TMEs), cellular jamming and poor vascularization produces gradients of oxygen levels, which can in turn play a distinct role in cell signaling or the responsiveness of immune cells such as macrophages. Furthermore, tumors with high hypoxia levels are known to be stiffer than those without.[37] However, answering many of these questions at a fundamental level requires being able to formulate tumor models that possess specific structural features. Tumors grown in mouse models are, like human tumors, complex and heterogeneous, and thus difficult to produce with controlled features such as varying hypoxia levels or mechanics to address specific biological questions. We demonstrate here methods to systematically modulate the microenvironment in 3D tumor spheroids by altering the DNA lengths between the cells.

First, based on prior work, DNA interactions were used to produce monoculture 3D spheroids from 4T1 mouse breast cancer cells using two different schemes (Fig. 1).[14,30] For this, the cells were first reacted with an epidermal growth factor (EGFR) binding affibody-streptavidin fusion protein. The photocrosslinkable affibody-streptavidin (N23BP-STV) was expressed with a terminal 6× histidine tag, purified using Ni–NTA affinity columns and reacted with maleimide-benzophenone (BP) to enable photocrosslinking to EGFR upon long UV irradiation. After reacting the N23BP-STV to 4T1 cells, 20 base pair (bp) biotinylated and FAM labelled DNA oligonucleotides were added and as shown in Fig. 2, after 4, 10 and 16 h, fluorescence was still easily detected in or on the outer surface of the cells. Despite a decrease in photoluminescence over time, signal was still observed at the cell membrane at 16 h. It should be noted that a decrease in fluorescence per cell might be due to the protein being endocytosed and lysed or cell proliferation occurring, thereby lowering the number of affibodies bound per cell.

Once it was established that the cells could bind the biotinylated single stranded DNA (ssDNA) and retain its expression, different lengths of biotinylated ssDNA were synthesized. Biotinylated ssDNA up to 100 bases was purchased commercially (Integrated DNA Technologies), but alternate techniques were needed to produce longer biotinylated ssDNA strands, such as 200 and 400 base DNA oligonucleotides. To achieve this, biotinylated 200 and 400 base pair single stranded DNA

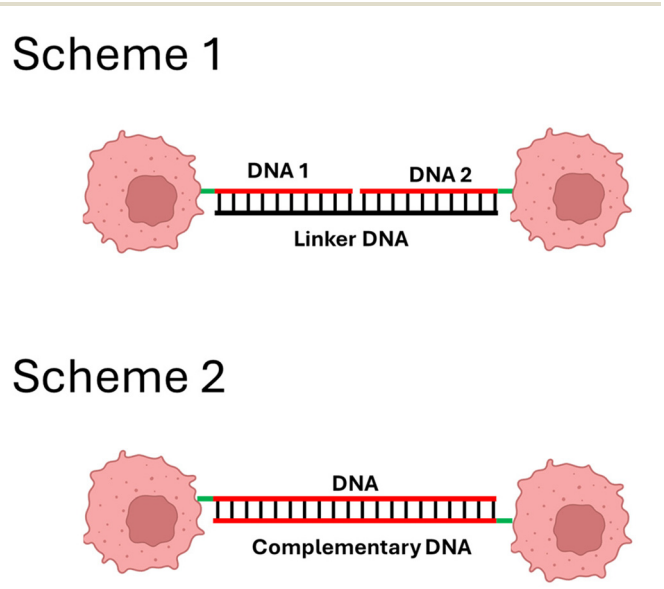

Fig. 1 Schemes to depict the two methods used to drive DNA interactions between cells. In Scheme 1, shorter DNA 1 and DNA 2 strands were hybridized to a 'Linker DNA' strand. In Scheme 2, two full complementary strands were attached to cells and hybridized.

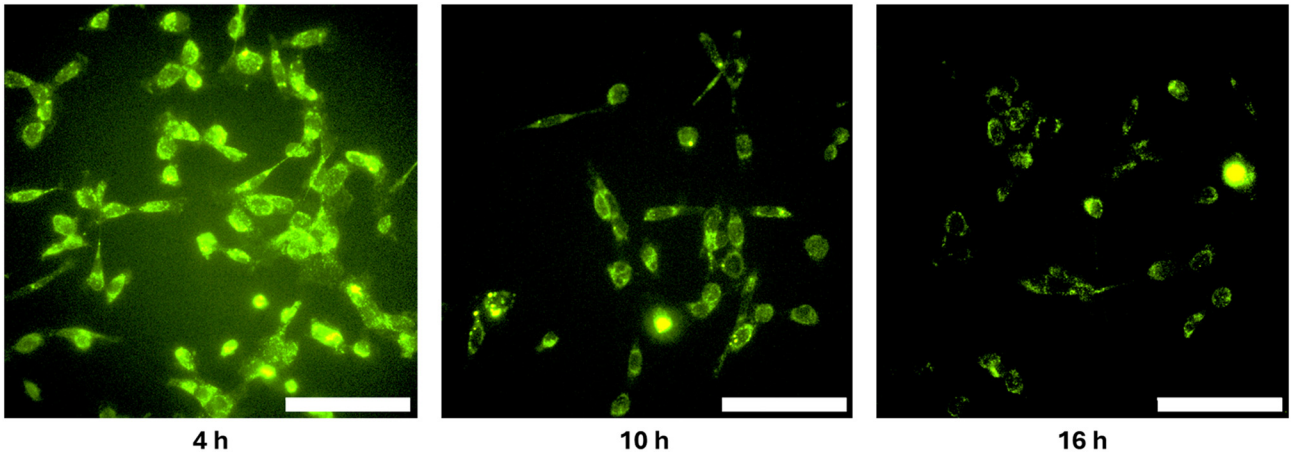

Fig. 2 Wide-field images of 4T1 cells after reacting with photocrosslinkable affibody-streptavidin fusion proteins followed by 20 base pair (bp) biotinylated and FAM labelled DNA oligonucleotides. Images shown are after 4 h of adding the FAM-DNA (left), 10 h (middle) and 16 h (right). Scale bar: 100 μm.

were first synthesized *via* PCR amplification of M13 phage ssDNA (New England Biolabs). The reason to use M13 ssDNA as the template strand was the lack of secondary structures within the circular ssDNA to enable efficient amplification of specific sequences.[38] To obtain the desired biotinylated single stranded DNA (ssDNA) to bind to the cells, one reaction used a biotinylated primer for one of the two DNA sequences and a phosphorylated primer for the complementary DNA strand (Tables 1 and 2, ESI Section†). In order to obtain ssDNA, the double stranded PCR DNA products were then purified using EZNA spin columns followed by digesting with the enzyme lambda exonuclease which selectively digests the phosphorylated DNA, leaving the biotinylated product intact. To confirm the existence of the correct length DNA strands, agarose gel electrophoresis was run with both 200 and 400 base pair products post-PCR and post-lambda exonuclease digestion (Fig. 3).

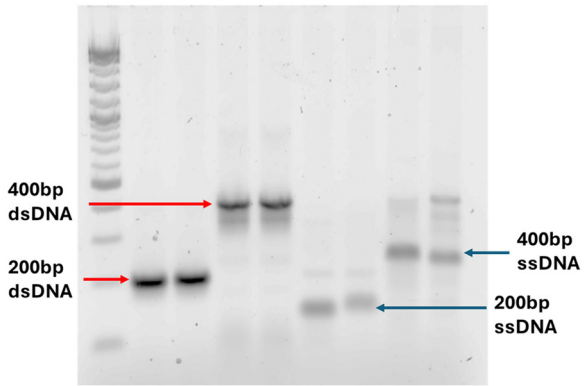

Fig. 3 Agarose gel electrophoresis of biotinylated double and single stranded DNA produced through amplification of specific regions in M13 ssDNA using biotinylated and phosphorylated primers. Singe stranded DNA (ssDNA) was produced after treating the PCR produced dsDNA with lambda exonuclease.

Next, to ensure that biotin was still present on the PCR generated ssDNA, the 200 base ssDNA and its complement were reacted with the affibody-streptavidin fusion protein for 4 h at 37 C and run through an agarose gel. A substantial decrease in brightness in lanes 5 and 6 (Fig. S1†) indicates that most of the biotinylated dsDNA associated with the affibody-streptavidin (N23BP-STV) and was therefore unable to pass through the gel. This result confirmed the presence of PCR produced biotinylated ssDNA. Next, the affibody-streptavidin (N23BP-STV) was photocrosslinked to 4T1 cells and reacted with non-dye labelled biotinylated 200 bp ssDNA. Concurrently, the equimolar amount of AF488-streptavidin was reacted with the complementary biotinylated single-stranded DNA sequences. As controls, cells not reacted with biotinylated ssDNA were used. After incubation, the cells were washed with PBS and then fixed on glass coverslips overnight and imaged. As shown in Fig. S2,† the experimental sample shows the signal coming from the AF488-streptavidin, while the control group shows limited fluorescence (aside from aggregates of AF488-streptavidin) indicating that hybridization between complementary strands occurs only if the initial biotinylated DNA were present on the cells.

Encouraged by our previous work,[14,30] we hypothesized that varying the DNA length would control the spacing between cells in the spheroid, which in turn would change cell packing density. Given that the extracellular EGFR domain is approximately 6 nm in diameter, and N23BP-STV consists of ~5 nm streptavidin and ~3 nm affibody, it is plausible that longer DNA strands could extend cell–cell contacts beyond the average length of 20–30 nm found for e-cadherin interactions.[39–42] To test these hypotheses further, 3D 4T1 spheroids were first formed using varying DNA lengths and 4T1 cells purchased from ATCC. For this, the biotinylated ssDNA with lengths were varying from 20, 100, 200, and 400 base pairs long were conjugated to the affibody-streptavidin modified cells. As controls, cells not reacted with DNA strands

were used. For the 20 and 100 bp ssDNA, Scheme 1 was followed while for longer strands, Scheme 2 was used (Fig. 1). First, the 4T1 cells were treated with 0.25–1 μM N23BP-STV in a 24-well TCPS plate, released, and treated with the varying lengths of biotinylated ssDNA chains in suspension. Following the incubation with ssDNA, the cells were seeded in 96-well poly-HEMA coated hemispherical plates followed by a 72–96 h incubation. As shown in Fig. 4, in all cases, compact 3D spheroids formed irrespective of the DNA length present on the surface of the 4T1 cells. In addition, MTT assays showed little to no change in cell viability using the different lengths of DNA (Fig. S3†). This finding is consistent with similar results run with DNA modified MDA-MB-468 cells in a previously published article.[30]

Next, studies were run to determine if any differences in cell matrix or cell–cell contacts were observed as a function of the DNA lengths used to assemble them. To perform this study, the formed spheroids were transferred to a flat imaging 96-well TCPS plate and left to adhere in an incubator. Once this step was completed, the 4T1 spheroids were fixed with paraformaldehyde (PFA), permeabilized with Triton-X100, blocked with bovine serum albumin (BSA), and stained with an AlexaFluor 488 conjugated anti-fibronectin antibody and an AlexaFluor 647 conjugated anti-e-cadherin antibody. After the staining was complete, the spheroids were cleared with RapiClear, imaged using the Nikon A1R confocal microscope, and processed in ImageJ. To obtain bulk quantitative information, a new set of spheroids not cleared with RapiClear were lysed with RIPA buffer overnight, sonicated, and the lysate fluorescence was measured. As shown in the images in Fig. 5, significant differences in brightness were not observed between any of the spheroids for either fibronectin or e-cadherin. Specifically, the fluorometry studies yielded bulk anti-e-cadherin intensities at 645 nm excitation and 671 nm emission of 58 100 ± 6510, 61 600 ± 7160, 61 500 ± 4640, 63 100 ± 6160, and 57 800 ± 1730 counts for no DNA, 20 bp DNA, 100 bp DNA, 200 bp DNA, and 400 bp for the formed DNA 4T1 spheroids. The *p*-value obtained through ANOVA single factor analysis was 0.720, which was insufficient to reject the null hypothesis. To further demonstrate this, a linear regression analysis was performed after transforming the dependent variable (Counts per μA) by taking the natural logarithm and the independent variable (DNA length) by taking the square root. The resulting significance factor of 0.918 was insufficient to

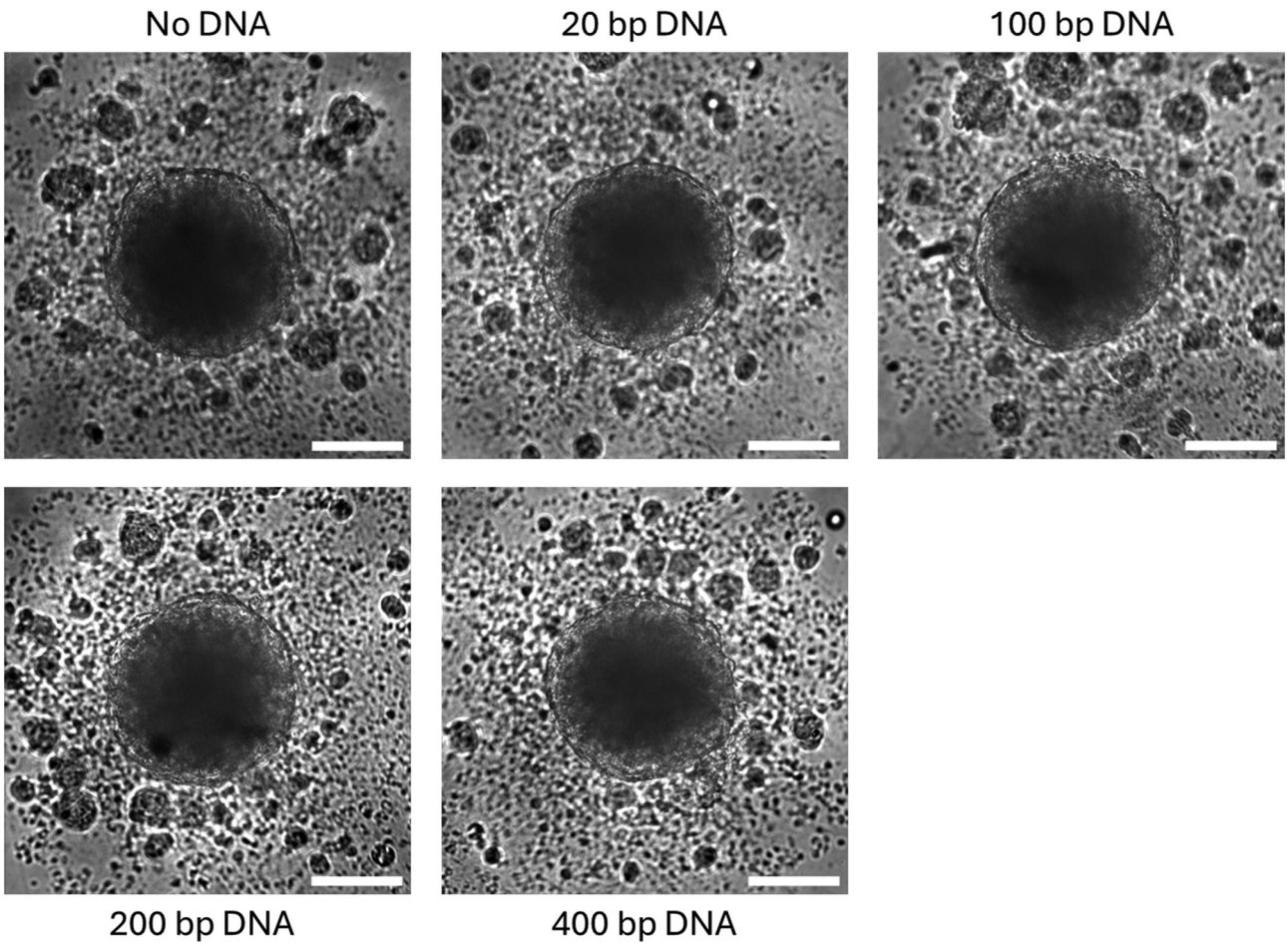

Fig. 4 Bright-field images of 3D 4T1 spheroids produced using varying DNA lengths. The average diameter of all the spheroids were ~310 nm irrespective of DNA length used. Scale bar: 150 μm.

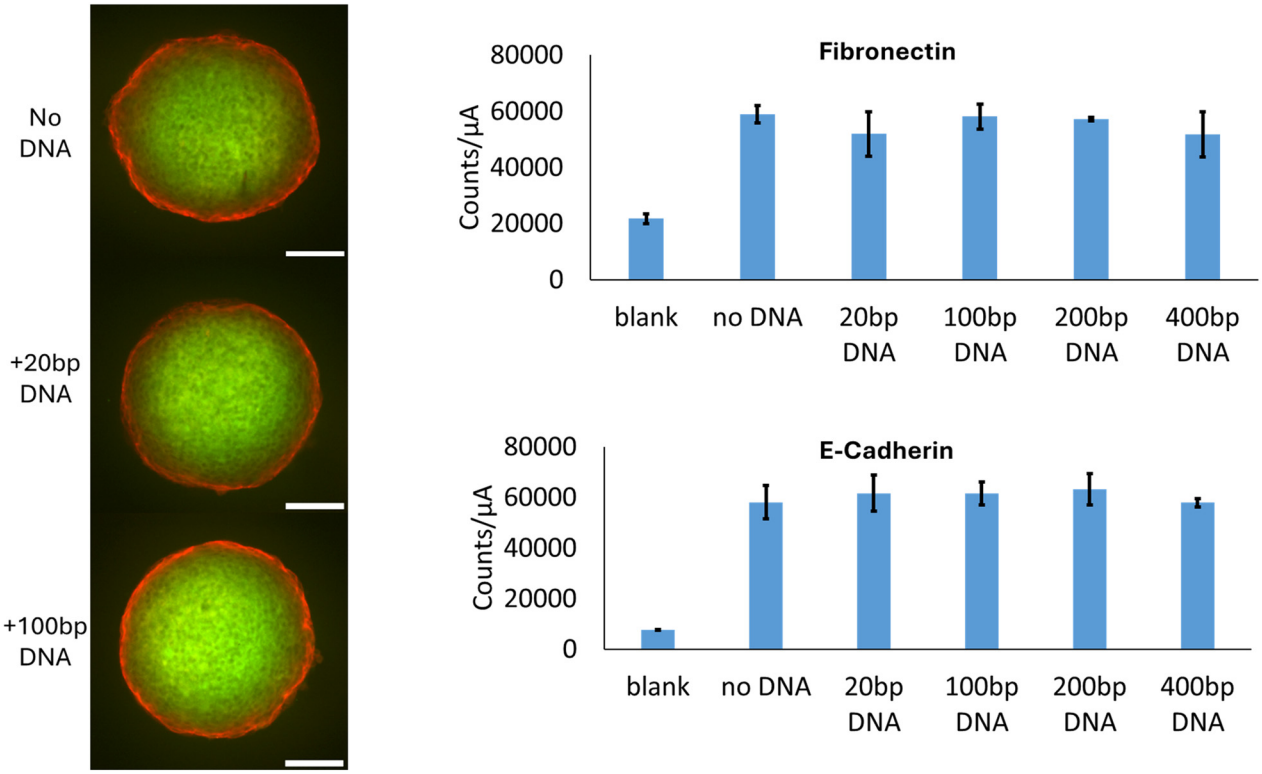

Fig. 5 Confocal and bulk fluorescence data obtained from 3D spheroids obtained using anti-cadherin and anti-fibronectin antibodies. *P*-Values for e-cadherin and fibronectin obtained through the ANOVA analysis were 0.720 and 0.385 respectively. The significance factors for e-cadherin and fibronectin obtained through the linear regression analysis were 0.918 and 0.419 respectively. Scale bar: 100 μm.

reject the null hypothesis. The background e-cadherin signal of the RIPA buffer was 7640 ± 105 counts. Similarly, the bulk fibronectin fluorescence at 470 nm excitation and 571 nm emission was 59 000 ± 3040, 51 900 ± 7940, 58 100 ± 4360, 57 200 ± 718, and 51 800 ± 8060 for no DNA, 20 bp DNA, 100 bp DNA, 200 bp DNA, and 400 bp DNA respectively. The *p*-value obtained through ANOVA single factor analysis was 0.385, which was insufficient to reject the null hypothesis. To further demonstrate this, a linear regression analysis was performed as described above. The background fibronectin signal of the RIPA buffer was 21 700 ± 172 counts. These results show that there is no significant difference between different DNA lengths when it comes to e-cadherin and fibronectin levels in 4T1 spheroids.

Next, the relative levels of hypoxia in each spheroid as a function of DNA length were determined. For this, 3D 4T1 spheroids were produced as a function of DNA length as described earlier. After 96 h, the fully formed spheroids were transferred to a flat imaging 96-well TCPS plate and left to adhere in an incubator. Once adhered, one of two staining processes was employed. In one, the spheroids were fixed with paraformaldehyde (PFA), permeabilized with Triton-X100, blocked with BSA, and stained with the AlexaFluor 488 conjugated hypoxia-inducible factor 1a (HIF1a) antibody (AF488-antiHIF1a). HIF1a is known to be upregulated in hypoxic environments and thus can be used as an indication of the relative oxygen levels in tissues.[17–23] As an alternative stain, another plate of 3D spheroids were live-stained with image-iT™ Hypoxia Green reagent (HYP), which converts to its fluorescent form at an increasing rate with increasing levels of hypoxia. For the HYP treated spheroids, the spheroids were treated with RapiClear after staining to enable deeper imaging into the spheroid. Next, both the AF488-antiHIF1a and HYP stained spheroids were imaged by confocal microscopy and processed by ImageJ. For quantitative fluorescence measurements from the images, a MATLAB code (see ESI†) was used to process the unmodified images to measure the average fluorescence intensity of the optical slice of the spheroid.

As shown in Fig. 6, the HYP stained 4T1 spheroids showed a clear drop in fluorescence with the addition of 20 base ssDNA and a continuous marked drop in luminescence with increasing DNA length. The quantitative processing with MATLAB further demonstrates this behavior, as fluorescence shows a decreasing trend with increasing DNA lengths. The lowest levels of hypoxia were observed in the 400 base pair spheroid sample with a mean pixel fluorescence intensity of 224 ± 9.12, while the highest levels of hypoxia were seen in the sample containing no DNA at 1180 ± 44.4, where the values are structured as mean ± standard deviation. 20 base pair, 100 base pair, and 200 base pair samples had intensities of 883 ± 74.7, 524 ± 65.5, and 313 ± 34.0 respectively. The ANOVA Single Factor *p*-value was 2.67×10^{-9}, which was sufficient to reject

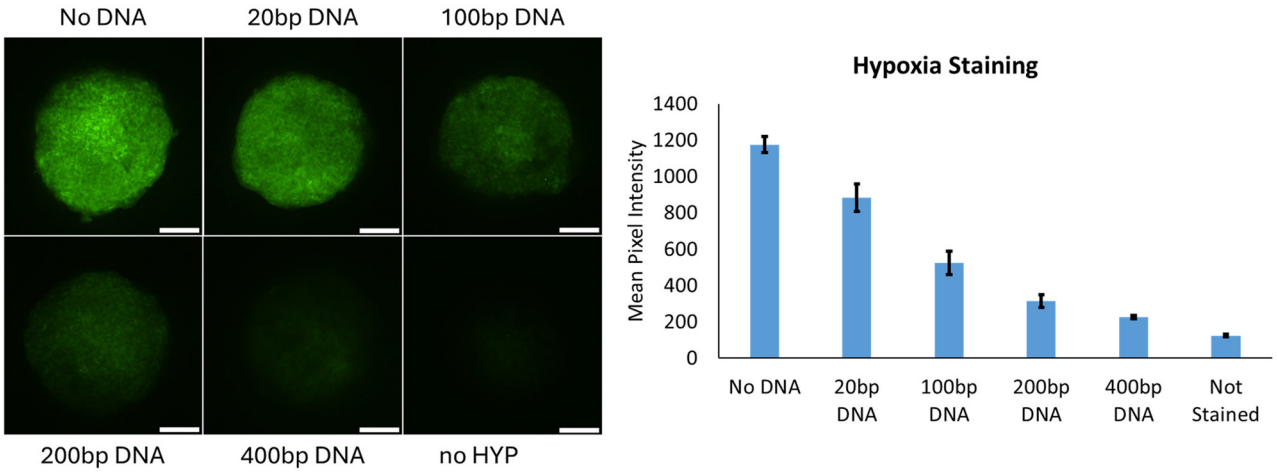

Fig. 6 (Left) Representative confocal images of spheroids made using different DNA lengths after treating with the hypoxia stain and RapiClear treatment. (Right) Bulk fluorescence data after MATLAB processing of spheroids made using different DNA lengths and treating with the hypoxia stain. The *p*-value obtained by the ANOVA was 2.67×10^{-9}. The significance factor obtained by the linear regression analysis was 9.69×10^{-9}. Scale bar: 100 μm.

the null hypothesis. To further demonstrate this, a linear regression analysis was performed after transforming the dependent variable (Mean pixel intensity) by taking the natural logarithm and the independent variable (DNA length) by taking the square root. The resulting significance factor of 9.69×10^{-9} was sufficient to reject the null hypothesis. It is worth noting that the need for optical clearing necessitated fixation and permeabilization of spheroids, which could have caused some of the HYP to leak out of them, potentially causing these results to not be fully in line with AF488 conjugated HIF1a antibody staining values.

To correlate the hypoxia data further, Fig. 7 shows the 4T1 spheroids stained with AF488-antiHIF1a with a similar decrease in HIF1a expression in the spheroids produced with increasing lengths of DNA. The highest levels of hypoxia were again observed in the spheroids produced using no DNA with a mean pixel fluorescence intensity of 724 ± 54.8, while the lowest levels were present in the 400 base pair DNA sample with an intensity of 318 ± 7.90. 20, 100, and 200 base pair samples had intensities of 521 ± 50.2, 376 ± 34.7, and 383 ± 25.7, respectively. The *p*-value obtained from the ANOVA Single Factor analysis was 1.01×10^{-6}, which was sufficient to reject the null hypothesis. To further demonstrate this, a linear regression analysis was performed after transforming the dependent variable (mean pixel intensity) by taking the natural logarithm and the independent variable (DNA length) by taking the square root. The resulting significance factor of 1.90×10^{-7} was sufficient to reject the null hypothesis. This result shows that diffusion of small molecules such as oxygen can be affected by cell surface modification with DNA chains

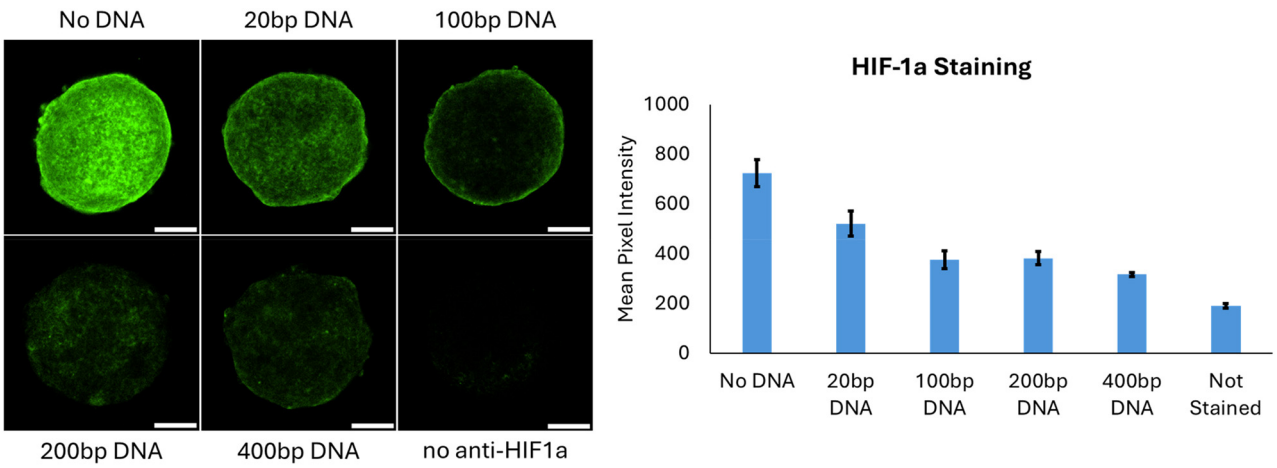

Fig. 7 (Left) Representative confocal images of spheroids made using different DNA lengths after fixing and treating with AF488-antiHIF1a. (Right) Bulk fluorescence data after MATLAB processing of spheroids made using different DNA lengths and treating with AF488-antiHIF1a. The *p*-value obtained by the ANOVA was 2.67×10^{-9}. The significance factor obtained by the linear regression analysis was 9.69×10^{-9}. Scale bar: 100 μm.

of different lengths, likely due to the increase in intercellular spacing and the porosity of the 4T1 spheroid, thus reducing the diffusion barrier for small molecules such as oxygen.

Lastly, to better determine the overall porosity of the formed 3D spheroids as a function of DNA length, the DNA-assembled spheroids were incubated with a non-cell reactive dye, rhodamine 6G. After 40 min incubation, the spheroids were washed, fixed, and imaged by confocal microscopy. As shown in Fig. S4,† a radial profile of the images obtained showed that the dye was able to penetrate further into the spheroids formed with 400 and 200 base pair DNA as compared to the 100 or 20 base pair DNA strands. This data is a rough estimate of the overall 'porosity' of the 3D spheroids as the difference between 400 and 20 base pair DNA is ~100 nm provided that the persistence length of DNA (~30 nm) holds.

Conclusions

In this study, we investigated the impact of varying DNA lengths on spheroid formation, cellular adhesion molecule expression, and hypoxia levels within 4T1 breast cancer spheroids. Through our experiments, we aimed to elucidate the potential of DNA-modified cell surfaces to regulate intercellular spacing and consequently alter hypoxia levels within the spheroid microenvironment. Our results demonstrated that modifying cell surfaces with biotinylated DNA strands of varying lengths facilitated spheroid formation without significant alterations in fibronectin and e-cadherin expression. This indicates that changes in DNA length did not significantly affect cellular adhesion molecule expression within the spheroids. However, our findings revealed a notable impact of DNA length on hypoxia levels within the spheroids. As DNA length increased, hypoxia levels decreased, suggesting that longer DNA strands led to increased intercellular spacing and enhanced porosity within the spheroid structure. This phenomenon likely facilitated the diffusion of small molecules such as oxygen, mitigating hypoxia within the spheroid microenvironment. Furthermore, our study underscores the importance of careful optimization and selection of staining techniques for accurate hypoxia detection within spheroids. We observed differences in staining patterns between reactive and non-reactive dyes, emphasizing the need for appropriate dye selection to ensure reliable results.

Overall, our findings contribute to the understanding of how DNA modification of cell surfaces can influence spheroid architecture and microenvironmental conditions. This study provides insights into potential strategies for modulating hypoxia levels within tumor spheroids, which could have implications for improving therapeutic interventions targeting the tumor microenvironment. As discussed earlier, the immunomodulatory response of cells such as macrophages incorporated within the tumors can be affected by the physiological microenvironment, including the relative levels of hypoxia. The studies shown here demonstrate methods to control the overall levels of oxygen in a 3D tumor model, which then can be used to study the effect on the phenotype of immune cells. The lessons from this study can perhaps educate or provide ideas of how to modulate the immune system response for cancer therapeutics. Further investigations are warranted to explore the broader applicability of DNA-based cell surface modification techniques in tumor biology and therapeutic development.

Materials and methods

The 4T1 cells obtained from ATCC were grown in Corning T-25 TCPS flasks in Gibco DMEM supplemented with 10% Gibco HI FBS, both from Thermo Fisher, in which the cells were grown to ~80% confluence. In addition, DMEM contained 1% HyClone Penicillin–Streptomycin antibiotic mixture from Cytiva, and 0.2% Plasmocin prophylactic from InvivoGen. Gibco DPBS from Thermo Fisher was used for washing cells, after which they would be detatched with Gibco TrypLE Express from Thermo Fisher. 15 mL conical tubes from Greiner Bio-One were used for cell spin-down and cell treatment with DNA. For N23BP-STV treatment, the 4T1 cells were grown in Corning 24-well TCPS plates. The N23C-STV was grown in NEB Lemo21(DE3) Competent *E. coli* transfected with N23C-STV plasmid, purified with Cytiva HisTrap HP 1 mL column, reacted with Chem Impex International 4-(Maleimido)benzophenone, and desalted with HiTrap Desalting 5 mL column. For purification, Fisher Scientific 10× PBS was used to prepare a stock of 1× PBS in Milli-Q water. Equilibration buffer, wash buffer, and elution buffer were made by adding Chem Impex Imidazole to PBS at 5 mM, 20 mM, and 250 mM concentration respectively. To prevent the formation of disulfide bonds within the N23C-STV, Research Products International TCEP (tris(2-carboxyethyl) phosphine) was added. 200 and 400 base pair DNA synthesis was performed using the primers obtained from Integrated DNA Technologies (IDT), and the Taq PCR Kit and M13mp18 Single-stranded DNA from New England Biolabs (NEB). The DNA purification was done using the E.Z.N.A. Cycle Pure Kit (V-spin) from Omega Bio-tek. The phosphorylated strand digestion was done using the Lambda Exonuclease from NEB. 20 and 100 base pair DNA was bought from IDT. After DNA treatment, spheroids were seeded in Fisher Scientific fisherbrand 96-well round bottom tissue culture plate coated with cell culture suitable poly(2-hydroxyethyl methacrylate) from Sigma-Aldrich. For imaging of HYP stained spheroids, and anti-fibronectin AF488 and anti-e-cadherin AF647 antibody-stained spheroids, 100 μL of RapiClear CS solution from SUNJin Lab was placed in each well. Anti-fibronectin AF488, anti-e-cadherin AF647, and anti-HIF1a antibodies were obtained from Santa Cruz Biotechnology, while the HYP stain was obtained from Thermo Fisher. To perform the Rhodamine 6G diffusion study, Rhodamine 6G was purchased from Thermo Fisher. MTT (3-(4,5-dimethylthiazol-2-yl)-2,5-diphenyltetrazolium bromide) needed for the cell viability study was procured from Thermo Fisher, while the sterile cell culture

tested dimethylsulfoxide (DMSO) necessary for dissolving the formazan crystals generated from the MTT by the cell metabolism was obtained from ATCC.

20 base pair DNA spheroid synthesis and hypoxia detection

Spheroids with 20 base pair DNA were synthesized according to the modified Ganguly *et al.* protocol.[30] First, the non-adhesive hemispherical 96-well plates were made by placing 100 μL of 30 mg mL^{-1} of poly-HEMA solution in 95% ethanol into each well that would have been used. These plates were allowed to dry for 48 h. To generate spheroids, the 4T1 cells were plated on a 24-well TCPS plate at 50 000 cells per well and were left to grow for 48 h. Once the incubation was complete, they were washed three times with PBS, treated with 500 μL of 0.5 μM solution of N23BP-STV in DMEM, and left at 37 °C and 5% CO_2 for 3 h. 4T1 cells were then irradiated with 365 nm UV light for 30 min and placed back in the 37 °C and 5% CO_2 incubator overnight. The next day, the cells were washed once with PBS, trypsinized, neutralized with DMEM, counted with a hemocytometer, spun down at 150 g for 5 min, and then dispersed to a concentration of 5 000 000 cells per mL. 3 solutions were then made, where one contained 4T1 cells at 50 000 cells per mL and 0.5 μM 20 base pair DNA 1, the other contained 4T1 cells at 50 000 cells per mL and 0.5 μM 20 base pair DNA 2, while the third solution contained 0.5 μM linker DNA (Scheme 1). These solutions were incubated at 37 °C and 5% CO_2 for 4 h, after which they were mixed at equal proportions, and 300 μL of this final solution was added to each poly-HEMA coated well in a hemispherical 96-well plate. After a 72 h incubation at 37 °C and 5% CO_2, they were transferred to an imaging 96-well TCPS plate and left to adhere to the surface overnight. For the image-iT™ Hypoxia Green reagent (HYP), the spheroids were washed once with PBS, and then left to react with 100 μL of 2.5 μM solution of HYP in DMEM for 1 h at 37 °C and 5% CO_2. Once this has elapsed, the spheroids were washed once with PBS and then left in 200 μL of FluoroBrite™ DMEM without FBS for 2 h at 37 °C and 5% CO_2 so the HYP dye could react and transition from its non-fluorescent to its fluorescent form. This medium was chosen to allow proteins that could fluoresce under 488 nm light to diffuse out of the spheroid, thus lowering background. Once the incubation was over, the 4T1 spheroids were washed twice with PBS, and fresh 200 μL of FluoroBrite™ DMEM was placed in wells. To stain the spheroids with the AlexaFluor 488 conjugated HIF1a antibody (AF488-AB), the spheroids were washed three times with PBS, and then fixed using 100 μL of 4% paraformaldehyde in water at room temperature for 20 min. Then, they were washed three times with PBS, and 100 μL of 0.5% TritonX-100 solution in water was placed and left in the wells for 15 min to permeabilize 4T1 spheroids. Once permeabilization was done, they were washed three times with PBS, and then blocked with 100 μL 3% bovine serum albumin solution in water for 1 h at 4 °C protected from light. After blocking, the BSA was taken out, and 100 μL of the 1 : 100 diluted AF488-AB antibody in 3% BSA was added to each spheroid containing well. The plate was then left to incubate at 4 °C protected from light overnight, and the next morning, the spheroids were washed 3 times in PBS, and 100 μL of RapiClear was placed in each well for imaging. The images were taken with Nikon AXR Confocal microscope using a PLAN APO λD 20x/0.80 ∞/0.17 WD 0.8 objective and a 488 nm laser line at a power of 95% and the detector gain of 45.0. The pinhole diameter was set at 64.4 μm (4 AU), using a 488 nm pinhole, and imaging was done at 2048 × 2048 resolution and a Galvano scanner. Images were processed with image J where the LUT was left unadjusted.

Biotinylated DNA synthesis

The enzyme used in the PCR was Taq PCR polymerase from NEB (E5000S). The reaction mixture was prepared according to the NEB protocol provided scaled up to 100 μL (cite this). The PCR cycle used for DNA synthesis was run with 30 s of initial denaturation at 95 °C, 50 cycles of 30 s of denaturation at 95 °C, 60 s of annealing at 51 °C, and 30 s of extension at 68 °C. Once these 50 cycles were completed, the final extension was run for 5 min at 68 °C, after which samples were cooled down and held at 4 °C. After the PCR, the DNA was cleaned by EZNA Cycle Pure kit spin columns from Omega Bio-Tek using the protocol provided by the manufacturer. At elution, 88 μL of DNA was gathered. Next, the purified DNA was digested by the lambda exonuclease from NEB (M0262S) using the protocol provided scaled up to 100 μL. After digestion, the product was ready to be used. The agarose gel electrophoresis was run with the 1% agarose gel containing EtBr to confirm the product at 100 V, 0.4 A, and 60 min for both DNA product confirmations and biotinylated DNA – N23BP-STV reaction product confirmation. The biotinylated DNA – N23BP-STV reaction was run at 37 °C for 4 h. The gels were imaged using the Cytiva Typhoon laser-scanner platform.

FAM DNA retention

4T1 cells used in this study were prepared by first seeding them on 12 mm diameter poly-L-lysine coverslips at 10 000 cells per well and incubating them at 37 °C, 5% CO_2 for 48 h. After the initial incubation, they were treated with 500 μL of 0.5 μM N23BP-STV in DMEM and left at 37 °C, 5% CO_2 for 3 h, irradiated under 365 nm light for 30 min, and incubated at 37 °C, 5% CO_2 overnight. The next day, the cells were reacted with 0.5 μM solution of biotin-DNA-FAM molecule in DMEM for 4 h. Once the reaction was completed, the cells were washed with PBS three times, and fresh DMEM was placed in 6 h and 24 h coverslip containing wells, while the 0 h coverslips were immediately fixed onto a glass slide using (find the brand of fixing agent). 6 h and 24 h coverslips were each washed 3 times with PBS and fixed onto a glass slide at their respective timepoints. The control samples were washed and fixed alongside the 0 h sample. Once the cells were fixed, they were imaged using the Nikon Widefield microscope with PLAN APO λ 40×/0.95 objective and 2048 × 2048 resolution, and a 16-bit Hamamatsu orca V3. They were illuminated with X-Cite XYLIS at 50% power using the GFP filter cube. The LUT was adjusted to 500–1450 interval for the AF488 channel and 3800–36 520 interval for the Hoechst channel.

DNA 1 – DNA 2 – linker binding

4T1 cells used in this study were prepared as mentioned in the paragraph above. When DNA treatment was done, the cells were treated with 500 mL of 0.5 μM biotinylated 50 base pair DNA 1 for 4 hours at 37 °C, 5% CO_2, while 100 μM AlexaFluor 488 conjugated streptavidin and 100 μM biotinylated 50 base pair DNA 2 were reacted at equal volume for 4 hours at 37 °C (reaction mixture). Control cells had their DMEM replenished and were not treated with DNA 1. Then, the reaction mixture was diluted in DMEM to 0.5 μM concentration of each constituent, and 100 base pair linker DNA was added to it at 0.5 μM (reaction solution). The cells on coverslips were then treated with 500 mL of 0.5 μM reaction solution for 2 hours at 37 °C, 5% CO_2. They were then washed 3× with PBS, stained with Hoechst for 10 minutes, washed again 3× with PBS, and fixed on glass slides overnight and protected from light with ProLong™ Glass Antifade Mountant. Once 4T1 cells were fixed, they were imaged using the Nikon Widefield microscope with PLAN APO λ 40×/0.95 objective and 2048 × 2048 resolution, and a 16-bit Hamamatsu orca V3. They were illuminated with X-Cite XYLIS at 50% power using DAPI and GFP filter cubes. The LUT was adjusted to 149–342 interval for the AF488 channel and 125–620 interval for the Hoechst channel.

Spheroid formation with different lengths of DNA

To generate 20 and 100 base pair DNA spheroids according to Scheme 1, the protocol described prior was used. Poly-HEMA plates were made using the protocol above. Making a stock of 4T1 cells at 50 000 cells per mL was described in the protocol above. To generate 200 and 400 base pair DNA spheroids according to Scheme 2, 3 solutions were made, where one contained 4T1 cells at 50 000 cells per mL and 0.01 μM DNA 1, the other contained 4T1 cells at 50 000 cells per mL and 0.01 μM DNA 2, while the third solution contained only DMEM. To make spheroids with no DNA present, 3 solutions were made, where one contained 4T1 cells at 50 000 cells per mL, the other contained 4T1 cells at 50 000 cells per mL, while the third solution contained only DMEM. All solutions had identical volumes. The incubation step, the solution mixing, the spheroid seeding, and incubation is described in the protocol above. Once the spheroids formed, they were imaged using Nikon Widefield microscope with PLAN APO λ 20×/0.75 objective and 2048 × 2048 resolution, and a 16-bit Hamamatsu orca V3.

Cell viability response to changing DNA modification lengths

To make a 4T1 cell suspension needed for the 2D plating, the protocols above related to the spheroid generation were used, up to and including the solution mixing. Once cell solutions were mixed, the DNA treated 4T1 cells were plated on a 96-well flat bottom imaging plate and incubated for 24 h at 37 °C and 5% CO_2. After incubation, the cells were washed three times with PBS and treated with 0.5 mg mL^{-1} of MTT in DMEM. They were left to incubate with the solution for 4 h at 37 °C and 5% CO_2. Next, the solution was carefully removed, and the crystals that formed were dissolved in DMSO for 15 minutes, and the resulting solution was gently mixed to remove potential concentration gradients within each well. Using the BioTek SYNERGY|H1 microplate reader, the absorbance of each well was measured at 650 and 560 nm, and the 560 nm absorbance was subtracted from the 650 nm absorbance to obtain the corrected absorbance value.

Fibronectin and E-cadherin response to changing DNA modification lengths

To make 4T1 spheroids for this study and to stain them with AlexaFluor 488 conjugated anti fibronectin antibody and an AlexaFluor 647 conjugated anti e-cadherin antibody, the protocols above related to spheroid generation, fixing, and immunostaining preparations were used. Once the 3% BSA blocking was complete, the spheroids were treated with these two antibodies overnight, after which they were washed 3 times with 200 μL of PBS. After washing, 100 μL of RapiClear was placed in each well for imaging, and the spheroids were incubated for 1 h at room temperature protected from light. The spheroids were imaged with the Nikon AXR Confocal microscope using a PLAN APO λD 20×/0.80 ∞/0.17 WD 0.8 objective, a 488 nm laser line at a power of 95% and the detector gain of 20.0, and a 640 nm laser line at a power of 95% and the detector gain of 20.0. The pinhole diameter was set at 103.7 μm (5 AU), using a 640 nm pinhole setting, and imaging was done at 2048 × 2048 resolution and a Galvano scanner. Images were processed with image J where the LUT was left unadjusted. For fluorimetry, another set of spheroids was prepared that was lysed with RIPA buffer for 72 h at 4 °C temperature protected from light after immunostaining. Once the incubation period has passed, the spheroids were completely homogenized using a dismembrator. Once homogenized, the bulk fluorescence of the solution was read using the HORIBA Jobin Yvon Fluoromax-3 Spectrofluorometer, where the samples were excited at 470 nm and the emission was read from 480 nm to 600 nm for Fibronectin (AF488 antibody). For E-cadherin (AF647 antibody), the samples were excited at 645 nm and the emission was read from 660 nm to 800 nm. Fibronectin emission peak occurred at 517 nm, while the e-cadherin peak occurred at 671 nm. The excitation and the emission slits were both set at 5 nm for the entirety of the detection.

Hypoxia response to changing DNA modification lengths

To make 4T1 spheroids for this study and to stain them with AF488-AB, they were prepared according to protocols above. Once they adhered to the 96-well flat imaging plate, they were prepared for immunostaining using the aforementioned protocol. Once the 3% BSA blocking was complete, the spheroids were treated with AF488-AB overnight, after which they were washed 3 times with 200 μL of PBS. After washing, 200 μL of PBS was placed in each well for imaging. The spheroids were imaged with the Nikon AXR Confocal microscope using a PLAN APO λD 20×/0.80 ∞/0.17 WD 0.8 objective and a 488 nm laser line at a power of 95% and the detector gain of 60.0. The pinhole diameter was set at 64.4 μm (4 AU), using a 488 nm pinhole setting, and imaging was done at 2048 × 2048 resolu-

tion and a Galvano scanner. Images were processed with image J where the LUT was left unadjusted.

To prepare 4T1 spheroids for this study and to stain them with HYP, the protocols described above were used. After staining, the spheroids were fixed with 100 μL of 4% PFA for 20 min at room temperature, washed 3 times with 100 μL of PBS, permeabilized with 100 μL of 0.5% Triton-X100 for 5 minutes, washed 3 times with 100 μL of PBS, and 100 μL of RapiClear clearing solution was placed in each well. The 4T1 spheroids were incubated with RapiClear for 1 hour, after which they were imaged with the Nikon AXR Confocal microscope using a PLAN APO λD 20×/0.80 ∞/0.17 WD 0.8 objective and a 488 nm laser line at a power of 95% and the detector gain of 45.0. The pinhole diameter was set at 64.4 μm (4 AU), using a 488 nm pinhole, and imaging was done at 2048 × 2048 resolution and a Galvano scanner. Images were processed with image J where the LUT was left unadjusted.

To obtain numerical data, the images for both HYP and AF488-AB were processed in MATLAB where a binary mask was made for each image and the average pixel intensity for each spheroid was taken. Once those values were obtained, the ANOVA single factor analysis was performed. Regression was performed on the linearized form of the equation $\ln y$ *vs.* $x^{1/2}$.

Rhodamine 6G penetration response to changing DNA modification lengths

To make 4T1 spheroids for this study and to stain them with rhodamine 6G, they were prepared according to protocols above. Once they adhered to the 96-well imaging plate, they were stained with a 5 μM solution of rhodamine 6G in FluoroBrite™ DMEM without FBS for 40 min. Once staining was complete, the spheroids were fixed for 1 h with 4% PFA after being washed twice with DPBS. Once the fixing was complete, they were washed twice with PBS, covered with 200 μL of PBS, and imaged with the Nikon AXR Confocal microscope using a PLAN APO λD 20×/0.80 ∞/0.17 WD 0.8 objective and a 514 nm laser line at a power of 12% and the detector gain of 1.0. The pinhole diameter was set at 16.9 μm (1 AU), using a 514 nm pinhole setting, and imaging was done at 2048 × 2048 resolution and a Galvano scanner. Images were processed with image J where the LUT was left unadjusted.

To obtain numerical data, the Rhodamine 6G images were processed in MATLAB where a binary mask was made and eroded to create a smaller mask. The smaller mask was subtracted from the original mask to obtain an annular mask for the average pixel intensity measurement of an approximately 10 μm wide layer from the original image. At the end of each loop, the smaller mask was then set as the original. This loop was repeated until the entire spheroid was divided into layers and each layer analyzed for its average pixel intensity.

Data availability

The data supporting this article have been included as part of the ESI.†

Conflicts of interest

There are no conflicts of interests to declare.

Acknowledgements

This work was funded by NSF 2025547. The confocal imaging work was performed at the BioFrontiers Institute's Advanced Light Microscopy Core (RRID: SCR_018302). The Nikon AXR Laser Scanning Confocal is supported by NIH Grant 1S10OD034320. The widefield imaging work was performed at the BioFrontiers Institute's Advanced Light Microscopy Core (RRID: SCR_018302). The Nikon Ti-E Widefield is supported by NIH grant R01CA107098S1. The agarose gel imaging work was performed at the Biochemistry Shared Instruments Pool. The Cytiva Typhoon 5 is supported by NIH Grant 1S10OD034218-01. We also thank help and assistance from Dr Joseph Dragavon and Nikolas Di Caprio.

References

1 K. E. de Visser and J. A. Joyce, *Cancer Cell*, 2023, **41**, 374–403.
2 N. M. Anderson and M. C. Simon, *Curr. Biol.*, 2020, **30**, R921–R925.
3 E. R. Molina, L. K. Chim, M. C. Salazar, S. M. Mehta, B. A. Menegaz, S.-E. Lamhamedi-Cherradi, T. Satish, S. Mohiuddin, D. McCall, A. M. Zaske, B. Cuglievan, A. J. Lazar, D. W. Scott, J. K. Grande-Allen, J. A. Ludwig and A. G. Mikos, *Acta Biomater.*, 2019, **100**, 38–51.
4 M. van de Wetering, H. E. Francies, J. M. Francis, G. Bounova, F. Iorio, A. Pronk, W. van Houdt, J. van Gorp, A. Taylor-Weiner, L. Kester, A. McLaren-Douglas, J. Blokker, S. Jaksani, S. Bartfeld, R. Volckman, P. van Sluis, V. S. W. Li, S. Seepo, C. Sekhar Pedamallu, K. Cibulskis, S. L. Carter, A. McKenna, M. S. Lawrence, L. Lichtenstein, C. Stewart, J. Koster, R. Versteeg, A. van Oudenaarden, J. Saez-Rodriguez, R. G. J. Vries, G. Getz, L. Wessels, M. R. Stratton, U. McDermott, M. Meyerson, M. J. Garnett and H. Clevers, *Cell*, 2015, **161**, 933–945.
5 N. Sachs, J. de Ligt, O. Kopper, E. Gogola, G. Bounova, F. Weeber, A. V. Balgobind, K. Wind, A. Gracanin, H. Begthel, J. Korving, R. van Boxtel, A. A. Duarte, D. Lelieveld, A. van Hoeck, R. F. Ernst, F. Blokzijl, I. J. Nijman, M. Hoogstraat, M. van de Ven, D. A. Egan, V. Zinzalla, J. Moll, S. F. Boj, E. E. Voest, L. Wessels, P. J. van Diest, S. Rottenberg, R. G. J. Vries, E. Cuppen and H. Clevers, *Cell*, 2018, **172**, 373–386.
6 S. M. Kirsh, S. A. Pascetta and J. Uniacke, in *The Tumor Microenvironment: Methods and Protocols*, ed. J. Ursini-Siegel, Springer US, New York, NY, 2023, pp. 273–285.
7 F. Perche and V. P. Torchilin, *Cancer Biol. Ther.*, 2012, **13**, 1205–1213.

8 F. Mittler, P. Obeïd, A. V. Rulina, V. Haguet, X. Gidrol and M. Y. Balakirev, *Front. Oncol.*, 2017, **7**, DOI: **10.3389/fonc.2017.00293**.
9 A. Agrawal, S. Lasli, Y. Javanmardi, D. Coursier, A. Micalet, S. Watson, S. Shahreza, B. Serwinski, B. Djordjevic, N. Szita, U. Cheema, S. Bertazzo, F. Calvo and E. Moeendarbary, *Mater. Today Bio*, 2023, **23**, 100821.
10 S. Chandrasekaran, H. Deng and Y. Fang, *Integr. Biol.*, 2015, **7**, 324–334.
11 C.-T. Kuo, C.-L. Chiang, C.-H. Chang, H.-K. Liu, G.-S. Huang, R. Y.-J. Huang, H. Lee, C.-S. Huang and A. M. Wo, *Biomaterials*, 2014, **35**, 1562–1571.
12 M. Rovere, D. Reverberi, P. Arnaldi, M. E. F. Palamà and C. Gentili, *Front. Bioeng. Biotechnol.*, 2023, **11**, DOI: **10.3389/fbioe.2023.1297644**.
13 H. J. Hwang, M.-S. Oh, D. W. Lee and H.-J. Kuh, *J. Exp. Clin. Cancer Res.*, 2019, **38**, 258.
14 S. A. Saemundsson, S. Ganguly, S. D. Curry, A. P. Goodwin and J. N. Cha, *ACS Biomater. Sci. Eng.*, 2023, **9**, 3185–3192.
15 C. Liao, X. Liu, C. Zhang and Q. Zhang, *Semin. Cancer Biol.*, 2023, **88**, 172–186.
16 B. M. Ortmann, *BMJ Oncol.*, 2024, **3**(1), DOI: **10.1136/bmjonc-2023-000154**.
17 N. Akakura, M. Kobayashi, I. Horiuchi, A. Suzuki, J. Wang, J. Chen, H. Niizeki, K. Kawamura, M. Hosokawa and M. Asaka, *Cancer Res.*, 2001, **61**, 6548–6554.
18 K. A. Brand and U. Hermfisse, *FASEB J.*, 1997, **11**, 388–395.
19 T. N. Seagroves, H. E. Ryan, H. Lu, B. G. Wouters, M. Knapp, P. Thibault, K. Laderoute and R. S. Johnson, *Mol. Cell. Biol.*, 2001, **21**, 3436–3444.
20 B. H. Jiang, F. Agani, A. Passaniti and G. L. Semenza, *Cancer Res.*, 1997, **57**, 5328–5335.
21 J. Chen, S. Zhao, K. Nakada, Y. Kuge, N. Tamaki, F. Okada, J. Wang, M. Shindo, F. Higashino, K. Takeda, M. Asaka, H. Katoh, T. Sugiyama, M. Hosokawa and M. Kobayashi, *Am. J. Pathol.*, 2003, **162**, 1283–1291.
22 D. Zagzag, M. Nomura, D. R. Friedlander, C. Blanco, J.-P. Gagner, N. Nomura and E. W. Newcomb, *J. Cell. Physiol.*, 2003, **196**, 394–402.
23 R. Bernards and R. A. Weinberg, *Nature*, 2002, **418**, 823–823.
24 S. Koontongkaew, *J. Cancer*, 2013, **4**, 66–83.
25 A. L. Doedens, C. Stockmann, M. P. Rubinstein, D. Liao, N. Zhang, D. G. DeNardo, L. M. Coussens, M. Karin, A. W. Goldrath and R. S. Johnson, *Cancer Res.*, 2010, **70**, 7465–7475.
26 D. Laoui, E. Van Overmeire, G. Di Conza, C. Aldeni, J. Keirsse, Y. Morias, K. Movahedi, I. Houbracken, E. Schouppe, Y. Elkrim, O. Karroum, B. Jordan, P. Carmeliet, C. Gysemans, P. De Baetselier, M. Mazzone and J. A. Van Ginderachter, *Cancer Res.*, 2014, **74**, 24–30.
27 J. Friedrich, C. Seidel, R. Ebner and L. A. Kunz-Schughart, *Nat. Protoc.*, 2009, **4**, 309–324.
28 F. Vakhshiteh, Z. Bagheri, M. Soleimani, A. Ahvaraki, P. Pournemat, S. E. Alavi and Z. Madjd, *J. Nanobiotechnol.*, 2023, **21**, 249.
29 S. C. Brüningk, I. Rivens, C. Box, U. Oelfke and G. ter Haar, *Sci. Rep.*, 2020, **10**, 1653.
30 S. Ganguly, S. Roy, A. P. Goodwin and J. N. Cha, *Biomater. Sci.*, 2021, **9**, 7911–7920.
31 C. A. Mirkin, R. L. Letsinger, R. C. Mucic and J. J. Storhoff, *Nature*, 1996, **382**, 607–609.
32 F. A. Aldaye, A. L. Palmer and H. F. Sleiman, *Science*, 2008, **321**, 1795–1799.
33 C. Mao, W. Sun, Z. Shen and N. C. Seeman, *Nature*, 1999, **397**, 144–146.
34 J. Li, H. Pei, B. Zhu, L. Liang, M. Wei, Y. He, N. Chen, D. Li, Q. Huang and C. Fan, *ACS Nano*, 2011, **5**, 8783–8789.
35 Y. Zhang and N. C. Seeman, *J. Am. Chem. Soc.*, 1994, **116**, 1661–1669.
36 S. M. Douglas, I. Bachelet and G. M. Church, *Science*, 2012, **335**, 831–834.
37 J. Yoo, B. K. Seo, E. K. Park, M. Kwon, H. Jeong, K. R. Cho, O. H. Woo, S. E. Song and J. Cha, *BMC Cancer Imaging*, 2020, **20**, 85.
38 P. W. K. Rothemund, *Nature*, 2006, **440**, 297–302.
39 S. Ståhl, T. Gräslund, A. Eriksson Karlström, F. Y. Frejd, P.-Å. Nygren and J. Löfblom, *Trends Biotechnol.*, 2017, **35**, 691–712.
40 T. D. Perez and W. J. Nelson, *Handb. Exp. Pharmacol.*, 2004, 3–21.
41 R. P. D. Bank, RCSB PDB – 5WB7, **https://www.rcsb.org/structure/5wb7**, (accessed 6 March 2024).
42 A. Kuzuya, K. Numajiri, M. Kimura and M. Komiyama, *Nucleic Acids Symp. Ser.*, 2008, **52**, 681–682.